

AD-A120 866

HEATER-GENERATED INTERMEDIATE-SCALE IRREGULARITIES;
SPATIAL DISTRIBUTION A. (U) AIR FORCE GEOPHYSICS LAB
HANSCOM AFB MA R C LIVINGSTON 22 JUN 82
AFGL-TR-82-0174

1/1

UNCLASSIFIED

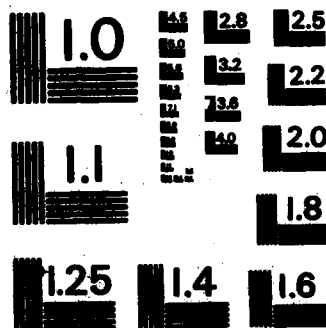
F/G 13/1

NL

END

Page 1

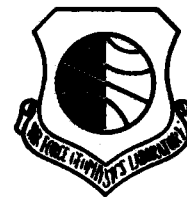
0000



MICROCOPY RESOLUTION TEST CHART
NATIONAL BUREAU OF STANDARDS-1963-A

AD A 120866

AFGL-TR-82-0174
ENVIRONMENTAL RESEARCH PAPERS, NO. 781



Heater-Generated Intermediate-Scale Irregularities; Spatial Distribution and Spectral Characteristics

ROBERT C. LIVINGSTON

22 June 1982

Approved for public release; distribution unlimited.

DTIC
ELECTE
OCT 29 1982
S D H

DTIC FILE COPY

SPACE PHYSICS DIVISION PROJECT 4643
AIR FORCE GEOPHYSICS LABORATORY
HANSCOM AFB, MASSACHUSETTS 01731

AIR FORCE SYSTEMS COMMAND, USAF



82 10 29 012

This report has been reviewed by the ESD Public Affairs Office (PA) and is releasable to the National Technical Information Service (NTIS).

This technical report has been reviewed and is approved for publication.


DR. ALVA T. STAIR, Jr.
Chief Scientist

Qualified requestors may obtain additional copies from the Defense Technical Information Center. All others should apply to the National Technical Information Service.

Unclassified

SECURITY CLASSIFICATION OF THIS PAGE (When Data Entered)

REPORT DOCUMENTATION PAGE		READ INSTRUCTIONS BEFORE COMPLETING FORM
1. REPORT NUMBER AFGL-TR-82-0174	2. GOVT ACCESSION NO. AD-A120 866	3. RECIPIENT'S CATALOG NUMBER
4. TITLE (and Subtitle) HEATER-GENERATED INTERMEDIATE-SCALE IRREGULARITIES; SPATIAL DISTRIBUTION AND SPECTRAL CHARACTERISTICS		5. TYPE OF REPORT & PERIOD COVERED Technical Report covering August 1980 to January 1981
7. AUTHOR(s) Robert C. Livingston *		6. PERFORMING ORG. REPORT NUMBER ERP No. 781
9. PERFORMING ORGANIZATION NAME AND ADDRESS SRI International 333 Ravenswood Avenue Menlo Park, California 94025		8. CONTRACT OR GRANT NUMBER(s)
11. CONTROLLING OFFICE NAME AND ADDRESS Air Force Geophysics Laboratory (PHY) Hanscom AFB Massachusetts 01731		10. PROGRAM ELEMENT, PROJECT, TASK AREA & WORK UNIT NUMBERS 62101F 464305AB
14. MONITORING AGENCY NAME & ADDRESS (if different from Controlling Office)		12. REPORT DATE 22 June 1982
		13. NUMBER OF PAGES 32
		15. SECURITY CLASS. (of this report) Unclassified
		15a. DECLASSIFICATION/DOWNGRADING SCHEDULE
16. DISTRIBUTION STATEMENT (of this Report) Approved for public release; distribution unlimited.		
17. DISTRIBUTION STATEMENT (of the abstract entered in Block 20, if different from Report)		
*Radio Physics Laboratory, SRI International, 333 Ravenswood Avenue, Menlo Park, CA 94025		
18. SUPPLEMENTARY NOTES Program Monitor: E.J. Weber This work was partially sponsored by the National Telecommunications and Information Agency under Contract NT80RAC06022. This work was partially supported under contract 74-5729 with Sandia Laboratories, Albuquerque, New Mexico 87185.		
19. KEY WORDS (Continue on reverse side if necessary and identify by block number) Scintillation Ionospheric heating		
20. ABSTRACT (Continue on reverse side if necessary and identify by block number) The first extensive phase scintillation measurements during both over- and underdense heating at Platteville are described. The data were collected from an aircraft, and by making repeated scans in the vicinity of the heated volume, the overall spatial distribution of intermediate-scale irregularities has been established. During overdense heating, the irregularities maximize in strength near the HF reflection height, but also map downward at least 100 km with only moderate weakening. From the relative frequency shifts of the phase spectra measured for different directions of aircraft motion, the irregularity		

DD FORM 1 JAN 73 1473

Unclassified


SECURITY CLASSIFICATION OF THIS PAGE (When Data Entered)

Unclassified

SECURITY CLASSIFICATION OF THIS PAGE(When Data Entered)

20. (contd)

anisotropy and drift have also been estimated. The change in phase spectral shape between 6.2 MHz and 9.9 MHz overdense heating is consistent with thermal self-focusing irregularity generation. Underdense heating produces a different phase spectral signature than is theoretically predicted, although enhanced energy does occur at scintillation producing scale sizes.



Unclassified

SECURITY CLASSIFICATION OF THIS PAGE(When Data Entered)

Preface

The author gratefully acknowledges the efforts of J. Buchau, J. Moore, A. Snyder, E. Weber (all AFGL), and C. Rush (NTIA) who planned the experiments; E. Violette and the other NTIA personnel who operated the heater; and R. Gowell and J. Waarmaa (both AFGL) who are always invaluable during the aircraft experiments. Thanks also to J. F. Vickrey and C. L. Rino for helpful discussions. The 4950th Test Wing operates the AFGL KC-135 airborne observatory.

Collection and preliminary analysis of the data was supported by the Air Force Geophysics Laboratory under Sandia Contract 74-5729.

3



Accession For	
NTIS GRA&I	<input checked="" type="checkbox"/>
DTIC TAB	<input type="checkbox"/>
Unannounced	<input type="checkbox"/>
Justification	
By _____	
Distribution/	
Availability Codes	
Dist	Avail and/or Special
A	

Contents

1. INTRODUCTION	7
2. EXPERIMENT BACKGROUND	9
3. PHASE SCINTILLATION CONSIDERATIONS	12
4. IRREGULARITY ANISOTROPY, DRIFTS, AND GEOGRAPHIC DISTRIBUTION	14
5. SPECTRAL CHARACTERISTICS DURING OVERDENSE HEATING	21
6. SPECTRAL CHARACTERISTICS DURING UNDERDENSE HEATING	25
7. CONCLUSIONS	29
REFERENCES	31

Illustrations

1. 300-km-altitude Heated Volume (circle) and Propagation Penetration Scans for Aircraft Flights on 13 and 16 October	10
2. Ionospheric FOF2 and Heater Operations on 13 and 16 October	11
3. Typical Phase Power Spectrum Obtained During Overdense Ionospheric Heating	13
4. Phase Power Spectra for Different Aircraft Flight Directions	16
5. Distributions of Phase Power Spectral Strength in Latitude and Longitude, Combined 13 and 16 October Data	18

Illustrations

6. Contour Map of Phase Power Spectral Strength, Combined 13 and 16 October Data, Relative to the Heated Volume (circle)	19
7. Long-term Behavior of 6.2-MHz Overdense Heating Phase Spectra, Main Heating Layer	22
8. Comparison of 6.2-MHz and 9.9-MHz Overdense Heating Phase Spectra, Main Heating Layer	23
9. Comparison of Overdense Heating Phase Spectra in Main and Secondary Irregularity Layers	26
10. Comparison of 6.2-MHz and 9.9-MHz Overdense Heating Phase Spectra in Secondary Irregularity Layer	27
11. Comparison of 6.2-MHz Overdense and 9.9-MHz Underdense Heating Phase Spectra	28

Tables

1. Overdense Thermal Self-Focusing	24
------------------------------------	----

Heater-Generated Intermediate-Scale Irregularities: Spatial Distribution and Spectral Characteristics

I. INTRODUCTION

Heating of the ionosphere by powerful high-frequency radio waves has been theoretically and experimentally studied for a number of years. It has been observed that in response to the elevated electron temperature that the heating creates, thermal processes and various instability mechanisms create a wide variety of electron density perturbations. These range in spatial scale from many kilometers through centimeters, and include the irregularities of interest to this report—the intermediate-scale (hundreds of meters to kilometers) striations that produce VHF-UHF radio wave scintillation.

Accumulated evidence suggests that the intermediate-scale irregularities arise from thermal self-focusing mechanisms. Weak background density variations distort the electric field of the propagating heater wave, enhancing its intensity at points of minimum electron density. This results in differential ohmic heating which, in conjunction with the field distribution, additionally drives ionization from already depleted regions. This process continues, amplifying the original perturbations, until hydrodynamic equilibrium is reached.

When the heating frequency is below the critical frequency of the F-layer (overdense heating), thermal self-focusing can create a layer of field-aligned

(Received for publication 25 June 1982)

irregularities near the altitude of the heating wave reversal.¹ Rapid thermal conduction and electric field mapping from the main energy deposition layer subsequently extend the irregularity region up and down the local magnetic field lines. The minimum cross-field dimension of the irregularities is dictated by the in-situ HF power density. Although the irregularities are only a few percent of the background density in strength, they can be anisotropic, and propagation along the extended field-aligned axis can produce significant VHF-UHF scintillation.

A somewhat different self-focusing process occurs when the heating frequency is above the F-layer critical frequency (underdense heating). Perkins and Goldman² have predicted the occurrence of weak sheetlike irregularities for in-situ power densities above a certain threshold. The sheets are oriented parallel to the plane determined by the heater beam and geomagnetic field directions, and have a cross-field width dependent on the heater frequency. The peak density perturbation of the sheets is also a function of heater frequency, and, accordingly, is low for HF excitation. However, as with the case of the overdense-heating-produced rods, significant VHF-UHF scintillation can occur for specific, along-sheet propagation geometries.

The first detailed study of heater-produced VHF and UHF scintillation was made at Platteville by Bowhill.³ Using spaced receivers, and both orbiting and geostationary signal sources, he characterized the spatial extent, anisotropy, and drift of overdense heating irregularities. More recently, Basu et al⁴ made similar measurements during a variety of heating conditions, and observed the first amplitude scintillation attributed to underdense heating. They also briefly describe airborne scintillation measurements made during the same heating periods. Since both the Bowhill³ and Basu et al⁴ experiments depended on signal amplitude measurements, the bulk of their quantitative results corresponds to near field-aligned propagation through the heated volume.

In this report we describe a scintillation experiment with a somewhat different emphasis. The observations presented are the first extensive complex signal measurements of heater-produced scintillation, and were made from an aircraft making relatively rapid scans of a large spatial volume. The importance of the

1. Perkins, F. W., and Valeo, E. J. (1974) Thermal self-focusing of electromagnetic waves in plasmas, Phys. Rev. Lett. 32:1234-1237.
2. Perkins, F. W., and Goldman, M. V. (1981) Self-focusing radio of radio waves in an underdense ionosphere, J. Geophys. Res. 86:600-608.
3. Bowhill, S. A. (1974) Satellite transmission studies of spread-F produced by artificial heating of the ionosphere, Radio Sci. 9:975-986.
4. Basu, S., Johnson, A. L., Klobuchar, J. A., and Rush, C. M. (1980) Preliminary results of scintillation measurements associated with ionospheric heating and possible implications for the Solar Power Satellite, Geophys. Res. Lett. 7:609-612.

complex signal measurement is that the phase of a transionospheric signal is generally unaffected by the propagation process for the frequencies and perturbation levels of interest here. The power spectral density function (SDF) of phase is therefore a nearly direct mapping of the in-situ irregularity continuum. Using phase measurements it is possible to determine small changes in the strength of irregularities as they are generated and as they drift and decay, and to observe the subtle changes in the irregularity spectral character produced under different over- and underdense heating conditions.

To take advantage of the experiment design we have concentrated our analysis on two particular aspects of our observations—the spatial distribution and drift of heater-generated irregularities, and the spectral character of those irregularities during various heating modes.

2. EXPERIMENTAL DESCRIPTION

The scintillation measurements that will be discussed were made aboard the Air Force Geophysics Laboratory AC-135A aircraft, which is also equipped for optical and ionospheric studies over the ocean.

For the scintillation measurements, a CW signal at 24.4 MHz from the geostationary ECHOSAT satellite was utilized. (ULF signals from the LKS-2 satellite were also received for these data, see sec. 4.1.1 of this report.) In Figure 2, the ionospheric propagation locations along the equator have been mapped for an altitude of 300 km. The last equator crossing, which was geostationary at 00°W, again occurred on the equator at about 40° elevation and 170° azimuth. For the largest elevation angle of 10°, these two angles correspond to a propagation angle of about 27° with respect to the magnetic field, so scintillation enhancement due to oblique wave propagation is small. A 100-km diameter heated volume (roughly the half-power beamwidth at 2 MHz and 300 km) is also indicated in Figure 2. The position of the heated volume much of the time during the 12 October night, or 13 October, the signal remained generally to the south of the heated beam.

The HF transmission schedule at Fitchville was chosen to provide overdense heating at two frequencies, 5.5 MHz and 2.5 MHz, and underdense heating at 0.8 MHz. The critical frequency, f_oF_2 , of the ionospheric F-layer, and thus the

5. Weber, R. J., Hunter, J., and Weber, J. C. Observations of equatorial F layer ionospheric irregularities. J. Geophys. Res. 66:4531-4541.

chosen pattern of heating, was nearly identical on both evenings of observations. These are shown in Figure 2; as can be seen, the heating was overdense until 0400 UT and underdense after that time.

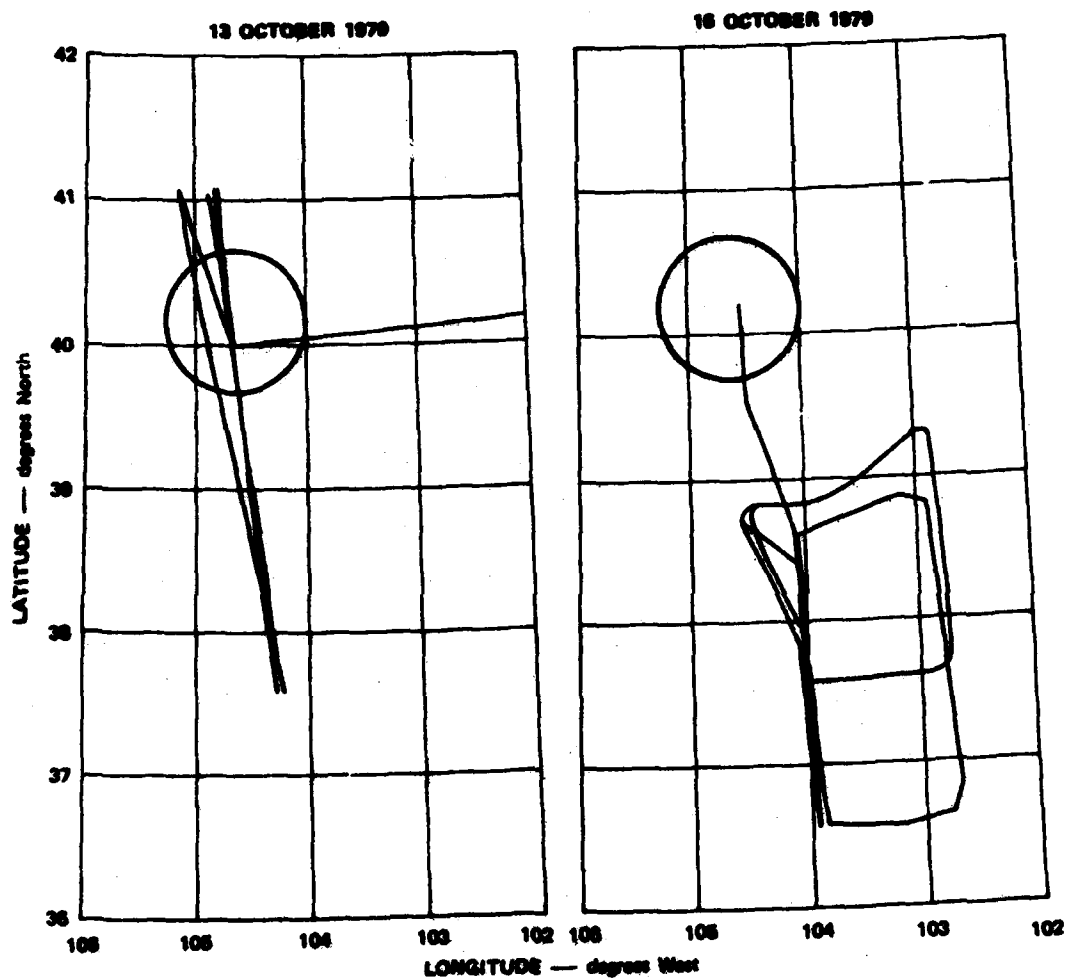


Figure 1. 300-km altitude Heated Volume (circle) and Propagation Penetration Scans for Aircraft Flights on 13 and 16 October

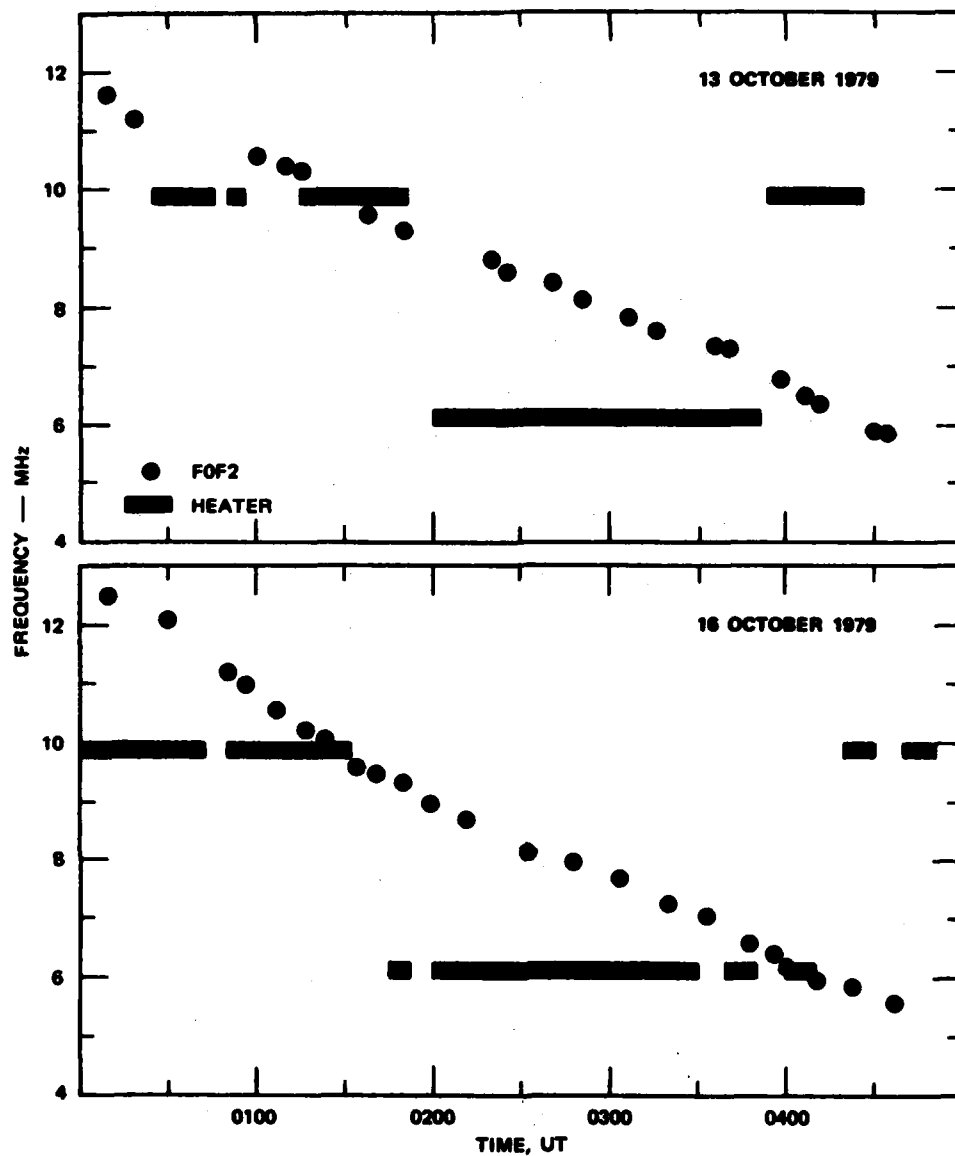


Figure 2. Ionospheric FOF2 and Heater Operations on 13 and 16 October

3. PHASE SCINTILLATION CONSIDERATIONS

The signal phase measurements used in the analysis are derived from precisely measured changes in received source frequency. As such, they include both dispersive (path-integrated ionospheric electron content) and geometrical (phase path length) components. When the propagation geometry is constant, the measured power spectrum of phase is a mapping of the in-situ spectrum, created as the irregularities drift through the propagation path. When the propagation geometry is changing, as it is with the aircraft, that same spectrum is shifted in frequency, due to a more rapid ionospheric scan, and is altered in magnitude and/or shape by the addition of geometrical phase energy. By and large, the geometrical contribution of aircraft motion to the phase spectrum occurs at low frequencies ($f < 0.01$ Hz) and is caused by slow deviations in the aircraft trajectory from straight and level flight.

The ionospheric processes at horizontal scale sizes exceeding several kilometers are not measurably altered by the heating process, and so are of little interest to our scintillation analysis here. However, we wish to avoid spectral contamination from these large-scale, large-magnitude density variations and to eliminate the slow phase deviations induced by aircraft motion. Accordingly, as the first step in analyzing the phase data, we make a spectral partitioning, removing low-frequency energy using a sharp-cutoff, high-pass filter. This results in a phase spectrum that includes contributions from intermediate-scale and smaller irregularities, that is, the regime altered by the heating process. A typical spectrum is shown in Figure 3. It is difficult to distinguish whether the spectrum is power-law in form, as is observed for moderate levels of naturally occurring scintillation, or Gaussian as would be suggested by the intensity scintillation results of Howhill.³ Spectra of this form, with similarly steep slopes, have been observed for weak levels of equatorial scintillation. We note that intensity scintillation is produced only by energy near the high-frequency end of this phase spectrum, which is very weak. This point will be discussed in more detail in the next section.

In portions of our analysis we deal directly with such spectra, but for morphological comparisons we have also characterized each one using log-log least-squares fits of the form

$$\phi(f) = Tf^p. \quad (1)$$

The spectral strength, T , and slope, p , provide a concise and convenient definition of the salient spectral character, and in a strict power-law environment

can be directly related to their in-situ counterparts.⁶ In practice, because the spectra are not continuously linear, the fitting process is applied over several adjacent and overlapped frequency ranges between 0.025 Hz and 0.5 Hz.

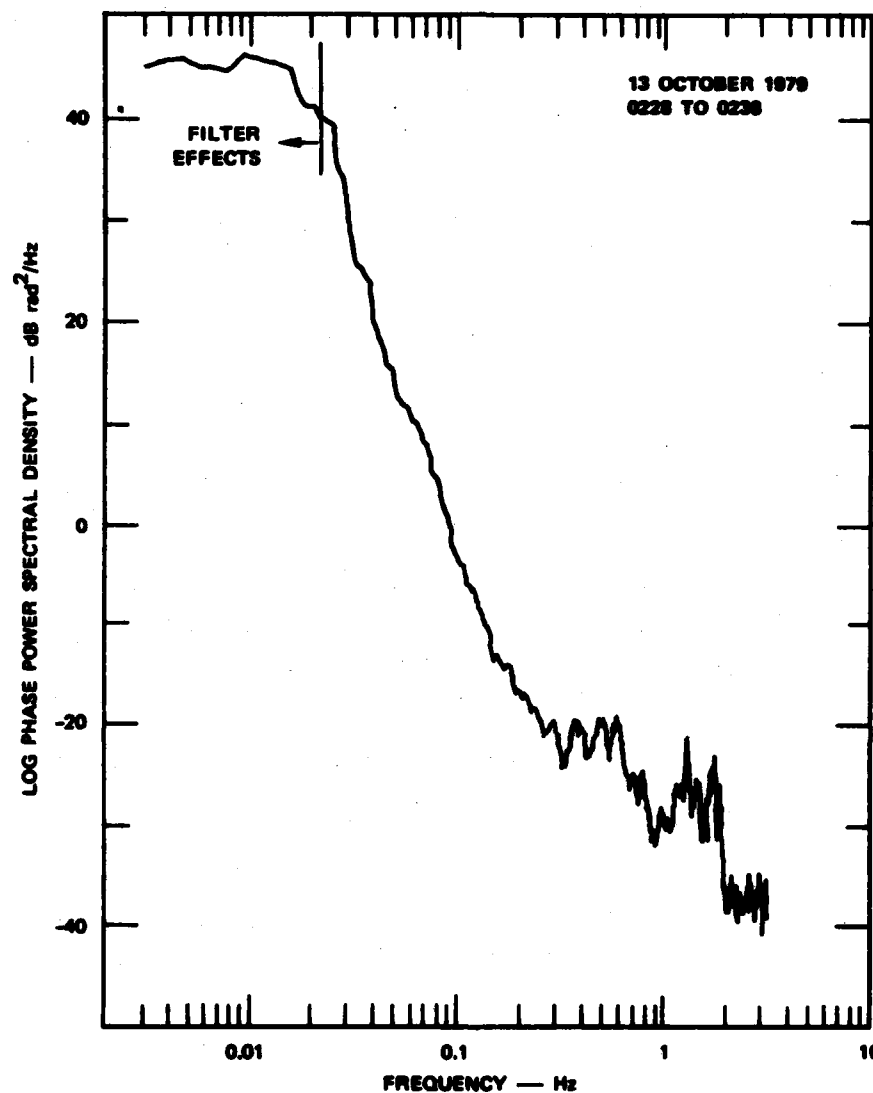


Figure 3. Typical Phase Power Spectrum Obtained During Overdense Ionospheric Heating

6. Rino, C.L. (1979) A power law phase screen model for ionospheric scintillation studies 1. Weak scatter, *Radio Sci.* 14:1135-1145.

Although the dominant contribution of aircraft motion to the phase spectrum is well below the frequencies of interest, more rapid aircraft motion can also add higher-frequency energy. The heater-produced phase scintillation is generally weak and is therefore susceptible to contamination or masking by this geometrical "scintillation." Prettie⁷ has calculated the phase spectral levels from aircraft vibration during normal cruise conditions. The vibration response of the aircraft is nearly flat over a range of 0.01 to 10 Hz and corresponds to a phase power spectral density of -25 dB rad²/Hz at 250 MHz. This, then, probably defines our noise floor, but is not a problem for the analysis at scintillation producing scales.

Of more concern is the aircraft motion induced by atmospheric turbulence. Fortunately, during the experiment flights, any significant turbulence was limited to a few short, isolated periods. To specifically determine the phase spectral character of the resulting aircraft motion, the data from one of those periods have been analyzed. We find that the aircraft motion produces a phase SDF that is also power-law, but with a shallower spectral index, p , and up to 10 dB higher spectral strength, T , than the heater irregularity phase SDF. In short, the spectra contaminated by aircraft turbulence are very conspicuous. With this in mind, several suspicious short data periods have been eliminated in the overall statistics.

4. IRREGULARITY ANISOTROPY, DRIFTS, AND GEOGRAPHIC DISTRIBUTION

One primary purpose of the aircraft observations at Platteville was to rapidly and repeatedly scan large regions of the ionosphere, and to thereby establish the geographic distribution of irregularities in the vicinity of the heater. The phase scintillation measurements are particularly well suited for this application because of their inherent sensitivity and because they relate directly back to irregularity turbulence strength. Furthermore, the phase spectra can be used to estimate irregularity drift speed and direction, which is an important factor in the long-term redistribution of heater irregularities outside the heated volume.

The mapping from in-situ irregularity spatial wavelengths to frequency in the observed temporal phase spectra is dictated by the effective aircraft propagation path scan and E×B-driven irregularity drift velocities. These two components add or subtract, depending on the aircraft heading with respect to the irregularity motion, causing slight frequency shifts in an otherwise constant phase power spectrum. In the case of east-west aircraft motion, the penetration-point scans are in a nearly cross-field direction at Platteville. Accordingly, the effective scan

7. Prettie, C.A. (1981) Phase Effects of Ionospheric Irregularities--Results of the Air Force Weight Aeronautical Data Processing Effort, Berkeley Research Associates Report.

velocity is independent of irregularity anisotropy, and is equal to the aircraft speed of ~ 200 m/s plus or minus the zonal irregularity drift. North-south aircraft motion is more nearly along the magnetic meridian, and for moderate to high irregularity axial ratios the aircraft motion contribution to the effective scan velocity is reduced to a value comparable to the in-situ drifts. This creates an interdependence of anisotropy and drifts that is complex, but calculable using the generalized expressions in Rino and Fremouw.⁸ We can then utilize the spectral frequency shifts caused by changes in effective scan velocity for different aircraft flight directions, to estimate not only the in-situ drifts, but also the irregularity anisotropy.

In Figure 4, spectra are shown for three consecutive legs of aircraft flight on 16 October in southward, eastward, and northward directions. All correspond to constant 6.2-MHz overdense heating in a region well removed from the primary heated volume, where the disturbance level is weak, but constant. For the range of frequencies of interest between 0.1 and 0.4 Hz, the north-south spectra nearly overlap one another while the eastbound spectrum is shifted upward in frequency. The information that can be gleaned from these data, when compared to the theoretical dependences on anisotropy and in-situ drifts, is threefold. Very briefly: (1) The separation between the northward and eastward spectra is consistent only with a narrow range of axial ratios near 5:1 for reasonable values of zonal drift. Axial ratios higher than this would quickly drive the two spectra apart. (2) The northward-eastward shift corresponds to a zonal in-situ drift of between 40 and 50 m/s eastward, depending on the meridional drift. (3) No shift between the northward and southward spectra implies a meridional drift component of 10 to 20 m/s southward.

We can compare these in-situ parameters with those previously observed. Anisotropy of heater-generated irregularities has never been studied in detail, although both Bowhill³ and Basu et al.⁴ found less decorrelation along-field than cross-field during spaced-receiver intensity measurements. This is consistent with our 5:1 axial ratio estimate. As for drifts, E-region conductivity will be low at the time of our observations, so our measured EXB drifts should be similar to the F-region neutral wind. This has been observed by previous experiments; [Bowhill,³ Duncan and Behnke,⁹ Basu et al.⁴]. In our case the drifts and neutral wind estimates match well in both magnitude and direction. For example, Hernandez and Roble¹⁰ found 25-m/s southward and 60-m/s eastward winds using

8. Rino, C. L., and Fremouw, E. J. (1977) The angle dependence of single scattered wavefields, *J. Atmos. Terr. Phys.* **39**:859-868.
9. Duncan, L. M., and Behnke, R. A. (1978) Observations of self-focusing electromagnetic waves in the ionosphere, *Phys. Rev. Lett.* **41**:998-1001.
10. Hernandez, G., and Roble, R. G. (1977) Direct measurement of nighttime thermospheric winds and temperatures 3. Monthly variations during solar minimum, *J. Geophys. Res.* **82**:5505-5511.

Fabry-Perot measurements (250-km altitude) from nearby Fritz Peak (39.9°N, 105.5°W) during the same season and local time. The global OGO-6 data/model of Hedin et al.¹¹ predicts similar southward, but somewhat stronger (75 m/s) eastward winds. In our data, then, we have direct confirmation that intermediate-scale, heater-produced irregularities drift with the nighttime background neutral wind.

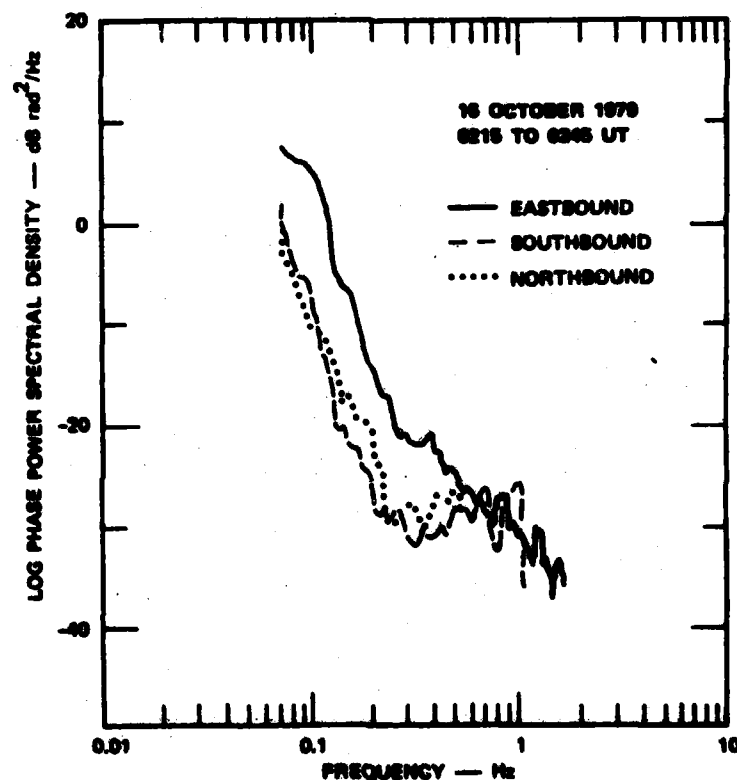


Figure 4. Phase Power Spectra for Different Aircraft Flight Directions

11. Hedin, A. E., Salah, J. E., Evans, J. V., Reber, C. A., Newton, G. P., Spencer, N. W., Kayser, D. C., Alcayde, D., Bauer, P., Cogger, L., and McClure, J. P. (1977) A global thermospheric model based on mass spectrometer and incoherent scatter data; MSIS 1, N_2 density and temperature, *J. Geophys. Res.* **82**:2139-2147.

The drift information can be utilized to produce accurate distributions of spectral strength with latitude and longitude. Basically, to directly compare values of T for different aircraft flight directions, the differences in effective scan velocity must be accounted for. Because our data consist mainly of many north-south legs, the correction is not essential, and it does not alter the general shape of the latitude and longitude distributions. Accommodating the drift reduces the scatter in the distributions and allows data from the east-west legs to be included. Since both the Hernandez and Roble¹⁰ data and the Hedin et al¹¹ model show that the early evening wind remains nearly constant, we have used the 0230 UT drifts to correct all of the 0200 UT to 0400 UT spectral strength data.

Figure 5 shows the distributions of spectral strength in latitude and longitude for the combined 13 October and 16 October data. Only the 6.2-MHz overdense heating periods (0200 UT to 0400 UT) have been included to ensure that the altitude of irregularity occurrence is consistent and identifiable (300 km). The Figure 5 data are referenced to the northbound 0.05-to-0.25 Hz spectral band (approximately 1500 m to 200 m cross-field spatial scales) although the data for the adjacent bands are very similar. The forms of the two distributions are quite similar. As expected, the irregularity strength peaks near the heater (40.16°N, 104.60°W), but decreases rapidly within about 100 km. Beyond that distance the irregularity strength declines more slowly.

We have also considered the distribution of spectral slope p in a similar manner, and found that it has a weak dependence on distance from the heater. In the vicinity of the heater, the average p is 5.5 for the 0.05-to-0.25-Hz spectral bin; far from the heater, p is 6.5. This slight steepening implies that the integrated energy in the spectral bin declines more slowly with distance from the heater than T does in Figure 5.

Much of the data spread in the distributions in Figure 5 is due to the mixing of latitudinal and longitudinal variations. To define the geographic distribution more clearly the data have been smoothed and mapped in Figure 6. On the map, the region of strongest disturbance is shifted slightly to the north of the heater volume. These two regions should coincide, and their misalignment suggests that the main overdense heating energy deposition is nearer 325 km than the 300 km we have assumed.

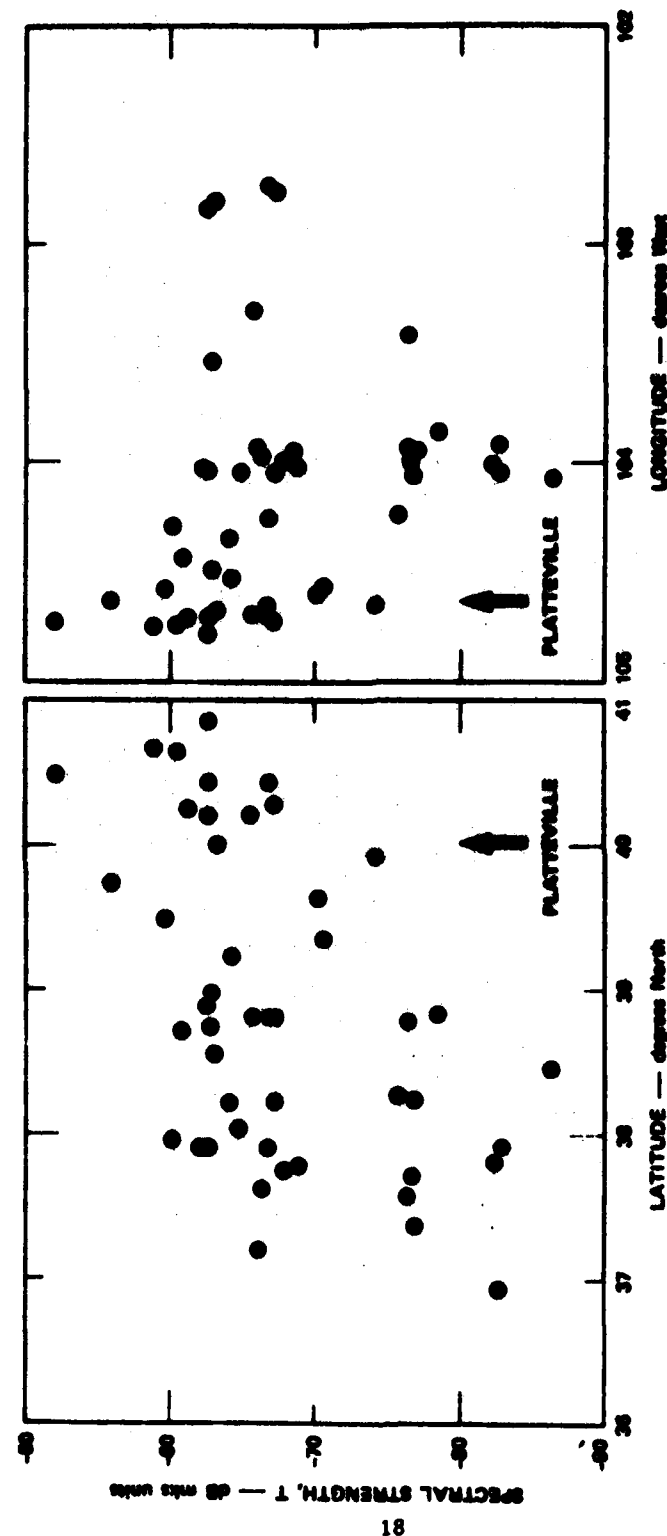


Figure 5. Distributions of Phase Power Spectral Strength in Latitude and Longitude, Combined 13 and 16 October Data

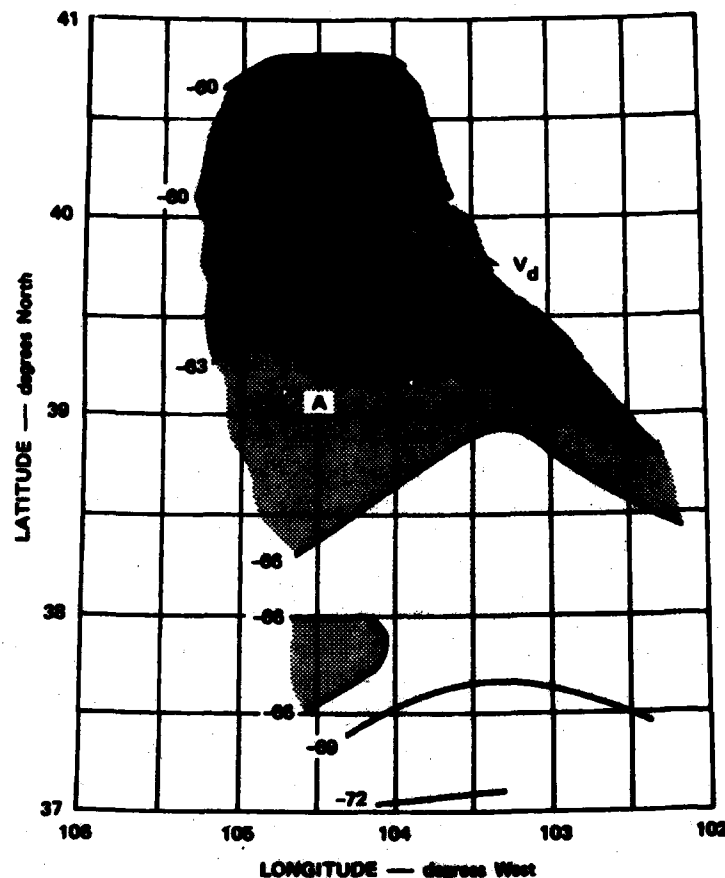


Figure 6. Contour Map of Phase Power Spectral Strength, Combined 13 and 16 October Data, Relative to the Heated Volume (circle)

The vector in Figure 6 indicates the irregularity drift direction. It is clear, from the alignment of that vector with the strength contours, that the drifts dominate the geographic distribution of irregularities that originate in the region of maximum heating. This is not surprising, based on the long lifetime (tens of minutes to hours) of the intermediate-scale structures.¹² There are drift paths of nearly 250 km from the main heated volume in Figure 6 over which the irregularities, overall, lose only 3 to 4 dB of energy. At a 50-m/s drift velocity, this implies an

12. Duncan, L. M. (1981) Ionospheric modification by high-power radio waves, Proceedings of the 1981 Symposium on the Effects of the Ionosphere on Radiowave Systems.

irregularity half-life of about 80 minutes. Implicit in this decay estimate is the assumption that the irregularity layer does not change thickness as it drifts from the heated volume. Unfortunately, we do not have measurements extending further downwind of the main heated volume to more precisely define a temporal decay rate.

Southeastward drift cannot explain the existence of irregularities directly south of the heater in Figure 6 that can be seen from the -66 dB and -69 dB contours near 38° latitude. This apparent southward distribution is evidence for a weaker irregularity region that extends downward in altitude from the primary 300-to-325-km layer. (Note that because the elevation angle to the satellite is 45° and the magnetic dip is 66°, irregularities mapped down the magnetic field appear south of the heater on the 300-km penetration map.) It has been observed¹³ that although overdense heating deposits energy in a thin layer near the altitude of wave reflection, rapid thermal conduction elevates electron temperatures both above and below that altitude. Perhaps more important for irregularity considerations, the perturbation electric fields set up by thermal self-focusing are mapped up and down along the magnetic flux tube passing through the heated volume. Our data can be used to estimate the irregularity strengths at these lower altitudes.

For penetration altitudes lower than 300 km, the contour pattern in Figure 6 shifts northward. For example, the point marked A centers over the heater for an assumed 200-km penetration height. This would imply that even 100 km below the reflection height, the overall irregularity strength is weaker by only 6 dB. A more detailed look at the efficiency of this downward irregularity mapping will be presented in the next section.

To conclude our discussion of irregularity morphology, some comments about intensity scintillation are appropriate. As previously pointed out, the spectral energy near the Fresnel zone radius (about 400 m for our frequency and geometry, or $f \sim 0.2$ Hz) is weak, even when the propagation path lies in the primary heated volume. The phase screen model⁶ has been applied using the spectral strength and slope extracted near 0.2 Hz during 8.2-MHz heating, and our observed anisotropy and drifts. The model predicts weak intensity scintillation, at a level of $S_4 = 0.13$, which is only slightly above the $S_4 \sim 0.10$ (1-1/2 dB fades) observed simultaneously through the heated volume from the ground (Rush, private communication). This latter value is near our measurement threshold, so a lack of conspicuous and systematic intensity scintillation from the aircraft is not surprising. In a later experiment, a level of $S_4 \sim 0.17$ (2.7 dB fades) was observed by Basu et al.⁴ for the same propagation geometry and heating at 9.9 MHz. It will be shown in the next

13. Mantas, G. P., Carlson, H. C., Jr., and LaHoz, C. H. (1981) Thermal response of the F-region ionosphere in artificial modification experiments by HF radio waves, *J. Geophys. Res.* **86**:561-574.

section that the irregularity scale sizes generated by thermal self-focusing depend critically on heating frequency and background ionospheric conditions. Thus we feel that there is no real discrepancy between our observations and those of Basu et al.⁴

We now turn from irregularity morphology to a study of the phase spectral slope dependence on heating frequency and mode.

5. SPECTRAL CHARACTERISTICS DURING OVERDENSE HEATING

As noted in Section 2, measurements were made during overdense heating at two different frequencies—6.2 MHz and 9.9 MHz. The accumulated statistics show that there are subtle differences in the phase scintillation between these heating periods, and in this section we consider the factors that contribute to those differences.

We first consider the measurements directly within the heated volume; this is the region of maximum irregularity strength, and thus maximum sensitivity for our spectral calculation. Furthermore, being within the heater beam, the observations are of the irregularities as they are being generated, and before they are distorted by drift or decay.

In Figure 7, these phase spectra for five different scans directly through the 6.2-MHz heated volume on 13 October are superimposed. All have been chosen to correspond to the same spatial volume and propagation geometry, and therefore are directly comparable. Three of the spectra obtained during northbound aircraft flight have been shifted to match the southbound frequency scale based on the observed irregularity drift (Section 4). During the more than two-hour period covered by the observations, the heating conditions were stable and constant; and, as expected, the five spectra are very similar in both form and magnitude over the long term.

An hour prior to the time of the first spectrum included in Figure 7 the same portion of heated volume was intercepted during 9.9-MHz overdense heating. The phase spectrum for that leg is shown in Figure 8 superimposed upon the combined 6.2-MHz spectra. The spectral difference between the two heating modes is conspicuous. The spectral energies are equal near 0.1 Hz but the spectral slopes are quite different—5.5 for 6.2 MHz and 3.5 for 9.9 MHz. As a result, above 0.3 Hz (cross-field spatial wavelengths shorter than about 250 m) the 9.9-MHz spectral energy is, on the average, some 5 dB stronger than that generated at 6.2 MHz. Conversely, at frequencies below 0.09 Hz (wavelengths greater than about 200 m) the 6.2-MHz spectrum dominates by 5 dB.

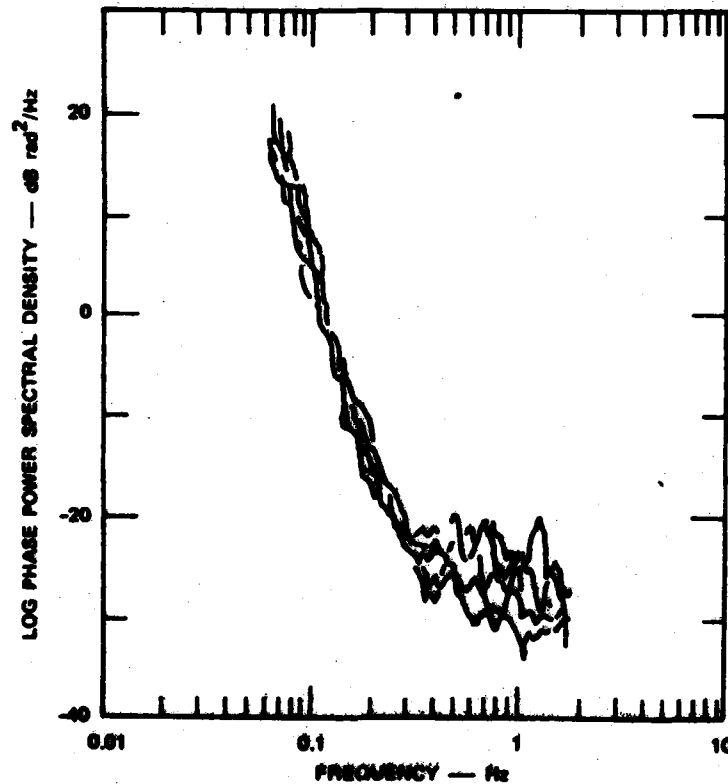


Figure 7. Long-term Behavior of 6.3-MHz Overdense Heating Phase Spectra, Main Heating Layer

We can compare this systematic shift in spectral energy caused by the change in heating frequency, to that predicted by theory. If, for the time being, it is assumed that the dominant irregularity generation mechanism during overdense heating is thermal self-focusing, the effective in-situ HF power density defines the threshold irregularity scale size.¹ In terms of experimental parameters, Duncan and Behnke⁹ express the threshold power density necessary to generate irregularities of cross-field dimension, λ , as

$$P \sim \frac{1.9 \times 10^{12} T_e^{1/2} \sin^2 \theta}{L f^3 \lambda^2} \quad (2)$$

T_e and L are the background electron temperature and plasma scale height, respectively, of the F layer. The HF heating frequency is f , and θ is the angle of heating incidence with respect to the local magnetic field.

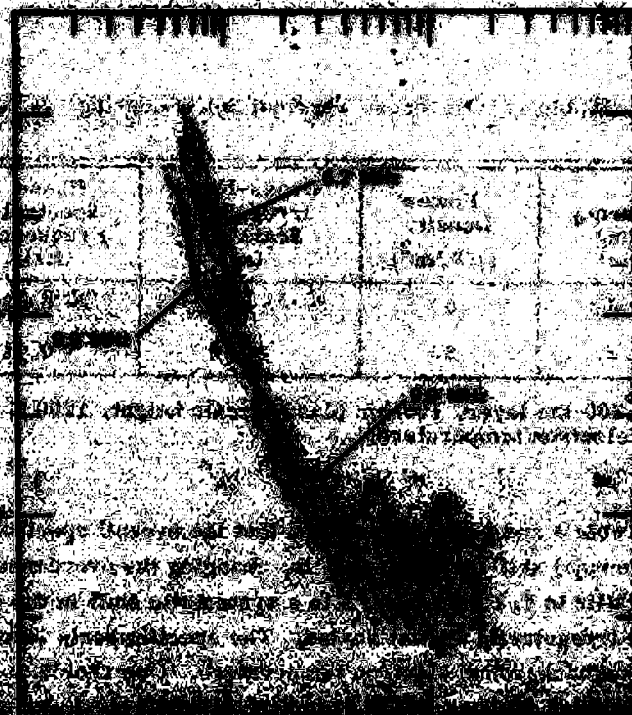


Table 1. Overdense Thermal Self-Focusing

Frequency Heating (MHz)	Power Density ($\mu\text{W}/\text{m}^2$)	Cross-Field* Irregularity Scale Size (m)	Phase Spectral Frequency (Hz)
9.9	69	> 350	< 0.23
6.2	62	> 750	< 0.11

* 300-km layer, 100-km plasma scale height, 1200 K electron temperature.

Comparing Table 1 and Figure 8, we find that the overall spectral behavior is consistent with thermal self-focusing, that is, changing the overdense heating frequency from 9.9 MHz to 6.2 MHz results in a systematic shift in the energy from shorter to longer irregularity spatial scales. The specific scale sizes listed are highly dependent on background electron temperature. Our choice of 1200 K, based on the moderate sunspot number, quiet geomagnetic conditions, and evening hours, appears to yield threshold scales consistent with our observations. However, the more steeply sloped 6.2-MHz spectrum ($p = 5.5$) suggests that the primary irregularity generation is at a single scale size near the self-focusing threshold, similar to the observations of Duncan and Behnke.⁹ On the other hand, the 9.9-MHz data exhibit a broader band of enhanced structure with a shallower slope ($p = 3.5$) at wavelengths larger than the threshold.

We can make similar 6.2-MHz and 9.9-MHz overdense comparisons for the "secondary" irregularities generated by energy mapped downward from the main heated layer. These create the scintillation observed at penetration locations directly south of the heater, as discussed in the previous section. The perturbation fields created by thermal self-focusing near the HF reflection height will map up and down the local magnetic field. The efficiency of that mapping is determined by the along- and cross-field conductivities, and the scale size of the source field.^{15, 16} The largest scale irregularity structures should therefore map to lower altitudes with little change, while those at the shortest scales will be weaker. We can check for this behavior in the phase spectra.

15. Farley, D. T., Jr. (1959) A theoretical study of electrostatic fields in a horizontally stratified ionosphere subject to a vertical magnetic field, J. Geophys. Res. **64**:1225-1233.

16. Farley, D. T., Jr. (1960) A theory of electrostatic fields in the ionosphere at nonpolar geomagnetic latitudes, J. Geophys. Res. **65**:869-877.

On 16 October, measurements were made south of the main heating penetration region, during 9.9-MHz overdense heating; shortly thereafter, another flight leg duplicated that geometry during 6.2-MHz heating. Figures 9a and 9b compare the phase spectra from these periods with those measured inside the heated volume. At frequencies less than 0.1 Hz (cross-field scale sizes larger than about 800 m) the upper and lower altitude spectra are virtually identical, indicating efficient downward mapping. Above this frequency, the spectra gradually diverge. For example, at $f = 1.0$ Hz (cross-field scale size of 80 m), the lower-altitude irregularities are weaker by about 10 dB. Both spectral pairs, at 6.2 MHz and 9.9 MHz, show the same depression of short scale size energy, so the mechanism is not peculiar to the heating frequency or mode. Most likely, then, the difference arises from scale-size dependent electric field mapping. In fact, if the main layer spectra can be assumed to be those of the irregularity generation process, the comparisons in Figures 9a and 9b could be used to define the functional dependence of cross- and along-field diffusion on scale size and altitude.

In Figure 10, the low-altitude spectra for the two heating frequencies are directly compared. The general distribution of spectral energy from high to low frequencies between 9.9-MHz and 6.2-MHz heating as predicted by thermal self-focusing still persists. So has the difference in spectral form: the 6.2-MHz spectrum is steeper ($p = 6.7$) than the 9.9-MHz spectrum ($p = 4.8$), although both have been distorted from those in the main heated layer by the lack of high-frequency (short scale size) energy.

We now consider phase spectral forms observed during underdense heating.

6. SPECTRAL CHARACTERISTICS DURING UNDERDENSE HEATING

On both 13 and 16 October, the ionosphere was heated at 9.9 MHz in an underdense mode following decay of f_0F_2 to below 6 MHz. For these underdense heating conditions, Perkins and Goldman² have predicted weak ($\frac{\delta n}{n} \sim 10^{-3}$) irregularity generation from thermal self-focusing at the power densities available at Platteville. These irregularities are sheet-like in form, with a cross-field dimension

$$\lambda = 1.2(15/f)^{1/2} \quad (3)$$

for typical F'-layer conditions, where f is the heating frequency in MHz or about 1450 m in the current case. At Platteville, the sheets are oriented vertically and along the magnetic field and for the FLTSAT observations are intersected at an angle of $\sim 20^\circ$.

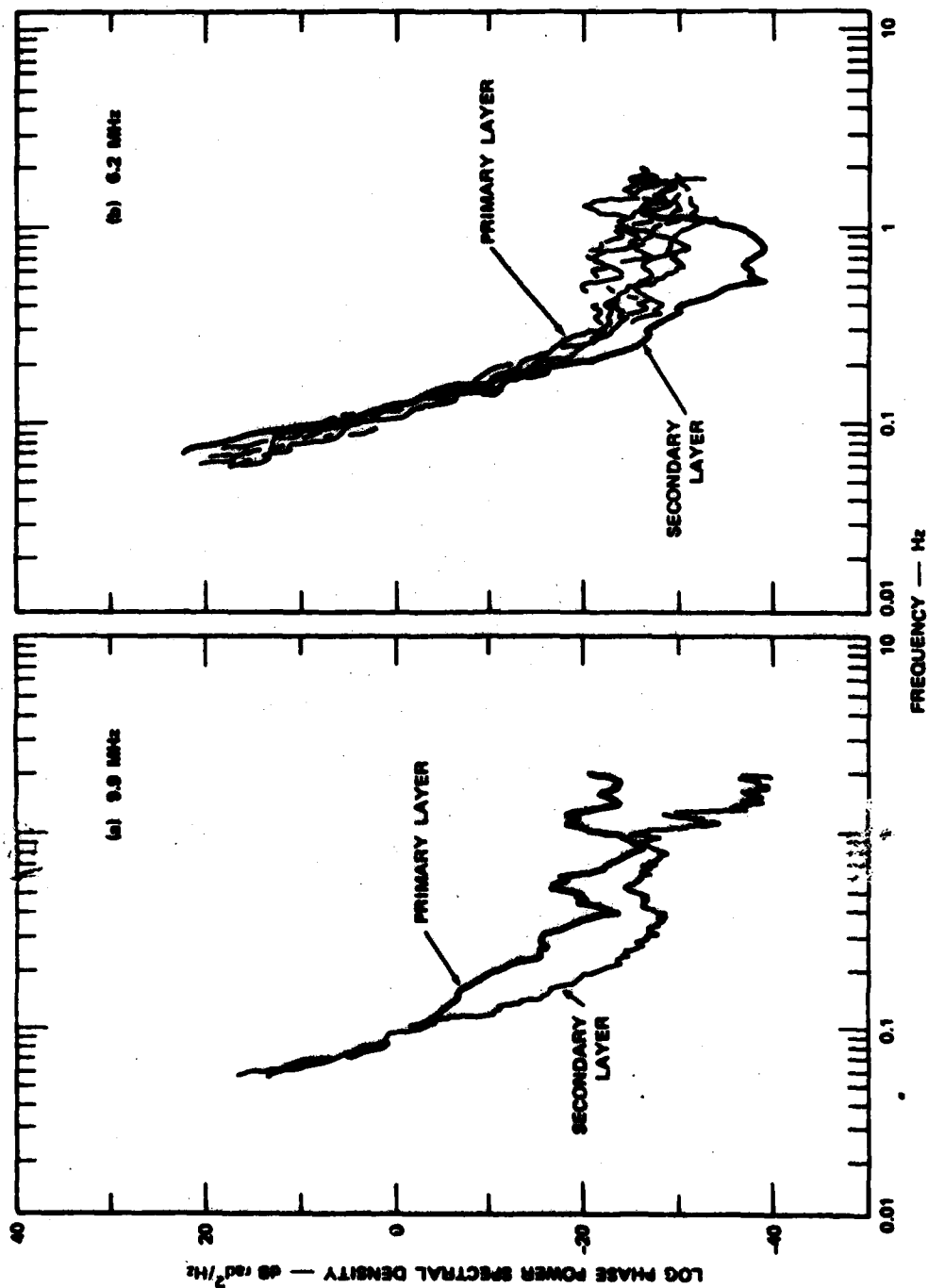


Figure 9. Comparison of Overdense Heating Phase Spectra in Main and Secondary Irregularity Layers

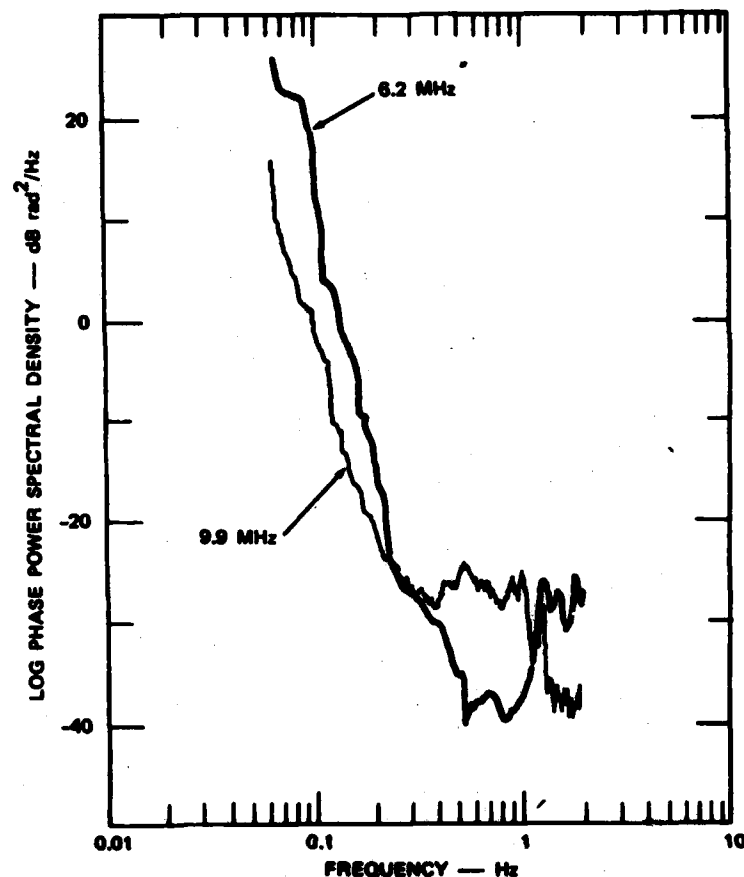


Figure 10. Comparison of 6.2-MHz and 9.9-MHz Overdense Heating Phase Spectra in Secondary Irregularity Layer

Perkins and Goldman² also predict a delay of about 1 min between underdense heater turn-on and observation of scintillation. During the 13 October flight that time occurred just as the penetration point passed through the F-layer peak altitude (350 km) directly over the heater. Presumably the underdense irregularity strength maximizes at the altitude of maximum density, and thus we obtained an ideal sampling for spectral analysis.

The phase power spectral density is shown in Figure 11. For comparison, a phase spectrum for 6.2-MHz overdense heating, also measured in the heated volume, is superimposed. The two spectra are separated by only 40 min in time

so that the background ionospheric conditions should be nearly constant. As discussed previously, the overdense heating should produce energy at frequencies below the 0.11-Hz threshold. For our propagation geometry and observed drifts, symmetrical sheets of 5:5:1 anisotropy and 1450-m cross-field dimension should appear near 0.05 Hz in the phase spectrum; less extended sheets will generate phase energy at slightly lower frequencies. In Figure 11, however, there is no distinguishable difference between the under- and overdense spectra near this frequency.

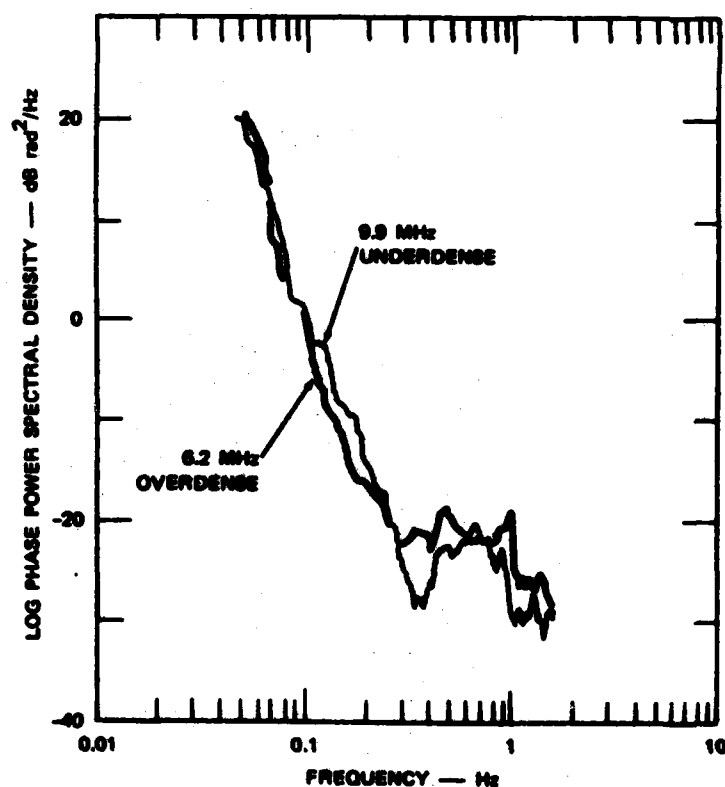


Figure 11. Comparison of 6.2-MHz Overdense and 9.9-MHz Underdense Heating Phase Spectra

It is difficult to conclude from Figure 11 that the Perkins and Goldman² mechanism is not operating. Only about 20 min separates the termination of

6. 2-MHz underdense heating and the underdense observation, much shorter than the large-scale irregularity lifetime. Thus, the match of the spectra below 0.1 Hz could be attributed to overdense heating residuals that mask the underdense produced sheets. Similar considerations apply to the energy in the underdense spectrum above 0.5 Hz where the levels are what might be expected for decayed, overdense residuals.

We note, however, that there is enhanced energy in the underdense spectrum between 0.1 and 0.3 Hz (cross-field spatial scales of 800 m to 260 m). A number of different explanations can be tendered for this occurrence. Secondary turbulent processes may quickly break down the sheets into smaller-scale irregularities. Alternatively, in addition to the single, maximum growth mode described by Eq. (3), a band of modes at shorter spatial scales may be produced by underdense heating. In any case, it is significant that the energy near the expected enhancement scale exceeds that in the overdense spectrum. This suggests that there are conditions under which intensity scintillation from underdense heating can exceed that for overdense heating. The likelihood of this occurrence is compounded by the sheet-like anisotropy of the underdense irregularities. Unlike the overdense produced rods, for which the scintillation maximizes for a unique, along-axis geometry, the sheets can enhance scintillation over a range of propagation angles.

From the current data set little can be learned about the underdense irregularity decay, mapping, or anisotropy. Certainly, additional underdense heating observations are warranted.

7. CONCLUSIONS

The complex signal measurements discussed in this report have confirmed and refined the experimental understanding of intermediate-scale heater-generated irregularities. We have taken advantage of the sensitivity of phase scintillation measurements, and the near-direct mapping of the irregularity spectrum that the phase data provide. Because of the sensitivity, the measurements are not limited to the particular (field-aligned) propagation geometries directly through the heated volume that are necessary to maximize intensity scintillation. The direct spectral mapping allows us to observe subtle changes in the irregularity power spectrum that occur with changes in heater mode and frequency. Finally, the airborne application of the measurements makes it possible to geographically map a large dynamic range of irregularity strengths and to determine the drift motion of those irregularities.

Our primary observations are as follows:

(1) The geographic distribution of intermediate-scale irregularities after long-term overdense heating has been directly measured. The irregularities are weak in terms of scintillation effects and maximize near the 300-km HF reflection height; in the vicinity of this region, their distribution is consistent with EXB drift of the irregularities from the heated volume. Using frequency shift information from the temporal phase spectra, irregularity anisotropy of near 5:1 and an east-southward irregularity drift of about 50 m/s have been inferred. As expected for the nighttime observations, this drift agrees well with previously established neutral-wind patterns. The temporal decay rate of the drifting irregularities is estimated to be 3 dB per 30 minutes. Enhanced irregularity strength at penetration locations south of the main heated layer, which cannot be explained by irregularity drift, indicate that the heater-produced irregularities, at least those at larger spatial scales, map downward more than 100 km in altitude.

(2) The phase spectra observed during overdense heating at two different frequencies are consistent with thermal self-focusing generation of intermediate-scale irregularities. The spectra are steeply sloped, averaging near f^{-5} over the intermediate-scale size regime. The form of the 6.2-MHz overdense spectra in the primary heated layer is remarkably constant over the long term, but a distinct shift in spectral energy occurs when the heating frequency is changed to 9.9 MHz. There is also a significant difference in the phase spectral slopes between the two heating frequencies, indicating that the simple model for thermal self-focusing irregularity generation is generally inadequate. The same spectral slope differences persist to the lower altitude regions to which the primary layer irregularities map, although the overall spectral forms are altered by the scale-size dependence of the mapping efficiency.

(3) Underdense heating does not appear to produce the selected scale-size enhancement predicted by theory, although this is difficult to verify because of slowly decaying residuals from prior overdense heating. There is, however, enhanced irregularity energy over a band of shorter spatial scales, which exceeds that generated during overdense heating.

Analysis of additional airborne scintillation data from Arecibo is currently underway, with an emphasis on further refining these observations.

References

1. Perkins, F.W., and Valeo, E.J. (1974) Thermal self-focusing of electromagnetic waves in plasmas, Phys. Rev. Lett. 32:1234-1237.
2. Perkins, F.W., and Goldman, M.V. (1981) Self-focusing of radio waves in an underdense ionosphere, J. Geophys. Res. 86:600-608.
3. Bowhill, S.A. (1974) Satellite transmission studies of spread-F produced by artificial heating of the ionosphere, Radio Sci. 9:975-986.
4. Basu, S., Johnson, A.L., Klobuchar, J.A., and Rush, C.M. (1980) Preliminary results of scintillation measurements associated with ionospheric heating and possible implications for the Solar Power Satellite, Geophys. Res. Lett. 7:609-612.
5. Weber, E.J., Buchau, J., and Moore, J.G. (1980) Airborne studies of equatorial F layer ionospheric irregularities, J. Geophys. Res. 85:4631-4641.
6. Rino, C.L. (1979) A power law phase screen model for ionospheric scintillation studies 1. Weak scatter, Radio Sci. 14:1135-1145.
7. Prettie, C.A. (1981) Phase Effects of Ionospheric Irregularities—Results of the Air Force Wright Aeronautical Data Processing Effort, Berkeley Research Associates Report.
8. Rino, C.L., and Fremouw, E.J. (1977) The angle dependence of single scattered wavefields, J. Atmos. Terr. Phys. 39:859-868.
9. Duncan, L.M., and Behnke, R.A. (1978) Observations of self-focusing electromagnetic waves in the ionosphere, Phys. Rev. Lett. 41:998-1001.
10. Hernandez, G., and Roble, R.G. (1977) Direct measurement of nighttime thermospheric winds and temperatures 3. Monthly variations during solar minimum, J. Geophys. Res. 82:5505-5511.
11. Hedin, A.E., Salah, J.E., Evans, J.V., Reber, C.A., Newton, G.P., Spencer, N.W., Kayser, D.C., Alcayde, D., Bauer, P., Cogger, L., and McClure, J.P. (1977) A global thermospheric model based on mass spectrometer and incoherent scatter data; MSIS 1, N₂ density and temperature, J. Geophys. Res. 82:2139-2147.

References

12. Duncan, L. M. (1981) Ionospheric modification by high-power radio waves, Proceedings of the 1981 Symposium on the Effects of the Ionosphere on Radiowave Systems.
13. Mantas, G. P., Carlson, H. C., Jr., and LaHoz, C. H. (1981) Thermal response of the F-region ionosphere in artificial modification experiments by HF radio waves, J. Geophys. Res. 86:561-574.
14. Rush, C. M., Violette, E. J., Espeland, R. H., Carroll, J. C., and Allen, K. C. (1980) Impact of SPS Heating on VLF, LF and MF Telecommunications Systems Ascertained by Experimental Means, U.S. Department of Commerce, Report NTIA-R-80-37.
15. Farley, D. T., Jr. (1959) A theoretical study of electrostatic fields in a horizontally stratified ionosphere subject to a vertical magnetic field, J. Geophys. Res. 64:1225-1233.
16. Farley, D. T., Jr. (1960) A theory of electrostatic fields in the ionosphere at nonpolar geomagnetic latitudes, J. Geophys. Res. 65:869-877.